Neural Computing and Applications
https://doi.org/10.1007/s00521-020-04897-5

ORIGINAL ARTICLE

A low-cost multichannel NIRS oximeter for monitoring systemic low-frequency oscillations

Yingwei Li[1,2] · Yunfei Ma[1] · Shaoqing Ma[1] · Lia Maria Hocke[2,4] · Yunjie Tong[3] · Blaise deB Frederick[2,4]

Received: 21 December 2019 / Accepted: 25 March 2020

Abstract
Systemic low-frequency oscillations (sLFOs) are non-neuronal oscillations at 0.01–0.15 Hz. These sLFOs travel through the entire body and the brain with symmetrical (across the midline of the body) and highly predictable delays, where they can be observed with functional near-infrared spectroscopy (fNIRS) and blood oxygen level-dependent functional magnetic resonance imaging. Their characteristics may serve as useful biomarkers for detecting and monitoring circulatory dysfunction. Pure sLFOs can be collected in the periphery (e.g., fingers, toes, earlobes). Here we present a 7-channel NIRS oximeter [MNO] for sLFOs detection and analysis in the periphery, which we named concurrent continuous wave fNIRS system (CON-CW fNIRS). Our CON-CW fNIRS is small ($10 \times 10 \times 20$ cm^3), highly portable, has low-power consumption and is highly cost-effective (below $300). We show that our device is highly reliable and can reproduce values acquired with a commercial fNIRS device with direct comparison (r_{max} = 0.908 Δ[HbO] and r_{max} = 0.841 Δ[Hb]) and when compared to previously published data.

Keywords fNIRS · Circulation · Systemic low-frequency oscillations · MSP430

1 Introduction

Low-frequency oscillations (LFOs: 0.01–0.15 Hz) are slow, spontaneous variations in hemodynamic parameters commonly observed in functional near-infrared spectroscopy (fNIRS) studies, where they are often interpreted as indicative of neuronal activity [1–6]. However, part of these LFOs is non-neuronal [1, 7, 8]. The origins and functions of these LFOs are complex and not fully understood [1]. In order to distinguish them from the neuronal LFOs, we refer to these physiological fluctuations as systemic LFOs (sLFOs). sLFOs with no neuronal components can be collected in the periphery at the fingers, toes and earlobes [9]. Frederick et al. have demonstrated strong correlations between the sLFOs collected in the periphery (NIRS) and in the brain (BOLD fMRI), with varying time delays [1]. These delays were symmetric across the body midline and demonstrate that some portion of sLFOs actually reflects systemic physiological circulatory effects. Furthermore, these sLFOs, and their temporal delays within the body and brain, can be reliably and consistently measured in healthy participants with predictable temporal ranges [1], which deviate in patients with restricted blood supply, such as moyamoya patients [10]. Therefore, sLFOs may serve as useful biomarkers for monitoring circulatory dysfunction or evaluating peripheral vascular integrity [1, 11].

For the aforementioned studies, a commercial fNIRS device (ISS Imagent, Champaign, IL) was used to detect sLFOs in the periphery of healthy subjects. However, commercial fNIRS instruments are not equipped with

✉ Yingwei Li
lyw@ysu.edu.cn

✉ Blaise deB Frederick
bbfrederick@mclean.harvard.edu

1 School of Information Science and Engineering, Yanshan University, Qinhuangdao 066004, Hebei, China

2 McLean Imaging Center, McLean Hospital, Belmont, MA 02478, USA

3 Weldon School of Biomedical Engineering, Purdue University, West Lafayette, IN 47906, USA

4 Department of Psychiatry, Harvard Medical School, Boston, MA 02115, USA

Published online: 08 April 2020

suitable probes for measurements of sLFOs in the periphery. Thus, custom probes were made by 3D printing technology, with a cumbersome manufacturing process and high experiment costs. Moreover, most commercial fNIRS instruments such as ISS, CW4, CW5 and CW6 system (TechEn Inc., MA, USA) [12–15] are designed and optimized for measuring the cerebral cortex. These instruments typically cost above $115,000 in dollars, are less than optimal for quick transport for concurrent studies, use high-cost laser emitters, photomultiplier tube detectors and utilize optical fibers to guide the optical signal. The latter does not only mean that users need to design optical fiber supports to affix the optical fiber to the peripheral tissues but also pose a problem with larger distances (e.g., distance between occipital and frontal cortex versus distance between earlobes and toes). Although the OxyMON system (Artinis Inc.) provides fiber length and stent customization services, the longer optical fiber is not ideal for measuring the peripheral tissues of fingers and toes [16–19]. To overcome this problem, Artinis has designed wireless portable device PortaLite NIRS system (Artinis Medical System, Elst, the Netherlands) to measure blood oxygen in muscles and transmit the data over Bluetooth [20, 21]. It contains one detector and three light sources, but the fixed distance between the detector and the light source cannot be flexibly applied in complex experiments [22, 23]. Although the dimensions of the wireless portable device are $84 \times 54 \times 20$ mm^3 and it weighs 88 g, it has only three channels, which is not enough to measure signals from multiple positions in the periphery [24].

The ETG-4000 and ETG-7000 (Hitachi Inc., Hitachi Medical Corporation, Tokyo, Japan) can adjust the position of the light source and detector and has 52 and 120 channels, respectively [25, 26]. These two instruments can simultaneously measure blood oxygen signals in multiple positions. However, they have unwieldy dimensions that are difficult to apply in complex experiments and research under task conditions [27, 28]. The dimensions of the NIRscout device (NIRx Medizintechnik GmbH, Berlin, Germany) are $260 \times 170 \times 330$ mm^3, with LED light sources and APD detectors, used for optical transmission and detection, respectively [29–31]. The equipment usually costs around $141,000, too much for many researchers to afford. NIRX has also developed a low-cost portable device called NIRsport (NIRx Medical Technologies LLC, Glen Head, NY, USA). It costs about $83,000 and has 55 channels per device [32, 33]. However, time-division multiplexing was adopted between the light source channels, and the channels are not all synchronized. When exploring sLFOs' propagation characteristics, it is necessary to explore the time delay and correlation coefficient of different measurement points in the peripheral position. This requires the different measurement points to achieve synchronous measurement [1], which in the case of the NIRsport is not the case and may lead to unpredictable errors in experimental results.

Based on the above analysis, the advantages of an energy-efficient, low-cost, highly portable device that can simultaneously measure sLFOs at multiple peripheral locations cannot be achieved by existing fNIRS devices. The concurrent continuous wave fNIRS system (CON-CW fNIRS) is proposed to measure sLFOs in multiple peripheral positions. Moreover, the portable design can be used for various measurements and task-based experiments and may serve as a monitor for circulatory dysfunction for clinical studies.

In this study, we compared our MNO device with the ISS (ISS Imagent, Champaign, IL) a commercial fNIRS device in order to verify the accuracy of our measurements, by direct comparison ($r = 0.908$ Δ[HbO] and $r = 0.841$ Δ[Hb]), displaying that the data collected by our MNO equipment have high reproducibility and are comparable to commercial fNIRS devices.

2 The system's operation principles

2.1 Basic acquisition principles of CW fNIRS

CW fNIRS is a neuroimaging technique for measuring changes in hemoglobin concentration. fNIRS takes advantage of the optical window, a range of wavelength from ~650 to 1200 nm in which the absorption spectra for human tissue favor oxy and deoxyhemoglobin over other chromophores in the tissue. Since smaller body parts and infant heads can be measured, the transmission mode, for adult heads, sources and detectors are positioned on the head approximately 3 cm apart in reflectance mode. After light is emitted from a source with at least two wavelengths within the optical window, the coupled light signal is absorbed and scattered by the tissue and collected by the detector. In the adult head, the photons collected by the detector travel a probability path, which spatially resembles a "banana shaped" between source and detector. This way, the light intensity signal's variation is obtained from the channel below the source and detector.

Most commercial CW fNIRS systems use the principle of time-division multiplexing (TDM), as shown in Fig. 1a. However, with the increase in the number of channels, the time required for the cyclic emission of the light source increases, which in turn decreases the overall sampling frequency. This may cause unnecessary errors when studying time delays of peripheral signals.

Light source modulation (MOD) is a method for improving the CW fNIRS system's temporal resolution. Modulating light sources into different frequency ranges

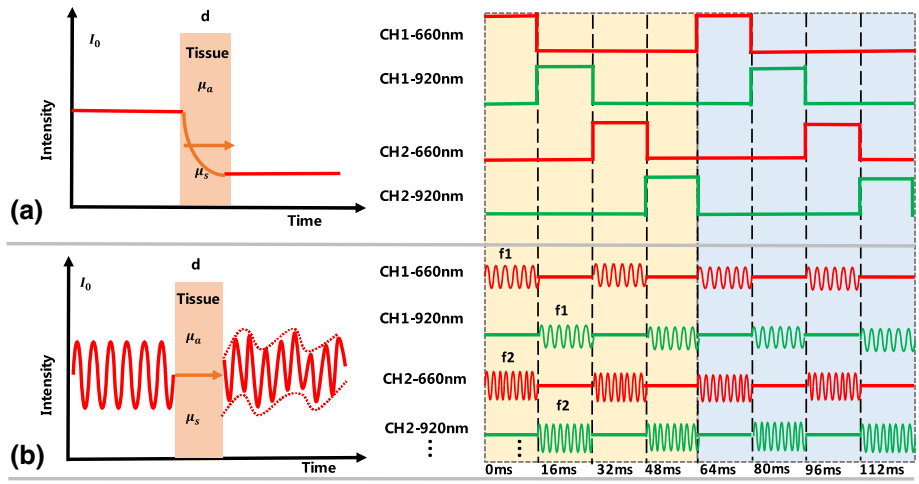

Fig. 1 Schematic diagram of the CW fNIRS system with **a** time division multiplexing (TDM) and **b** the light source modulation (MOD) CW fNIRS system

for transmission compensates for some of the traditional multi-channel CW fNIRS system's lower temporal resolution with multiple channels. MOD-CW fNIRS technology can be used with two different methods combined with time division multiplexing. The first method allows light sources from different channels with the same wavelength or light sources with different wavelengths from the same channels, to modulate at the same frequency. Because time division multiplexing is used between different channels, this method limits the number of extended channels. In the second method, the light sources from different channels with the same wavelength are modulated at different frequencies, and the time division multiplexing is used in the same channels, as shown in Fig. 1b. Although the second method overcomes the shortcomings of limiting the number of extended channels, it has a higher problem of crosstalk. When the sources of adjacent channels emit simultaneously, detectors of these channels can collect signals from multiple sources at the same time. In order to reduce crosstalk as much as possible, it is usually required that the spacing between carrier frequencies $f1$ and $f2$ is much larger than the signal's bandwidth. The frequency of the modulated light sources far exceeds that of the ambient light (50/60 Hz). Therefore, the bandpass filter can filter the ambient light better and prevent ambient light interference. However, the additional modulation and demodulation circuitry requires an increase both in the volume and in the cost of the system. Fortunately, in the case of the MNO, we can use mechanical separation to isolate the channels. By making measurements at remote peripheral locations, we can significantly decrease the multiplexing complexity, as only wavelengths need to be separated.

2.2 A CON: CW fNIRS proposal

Six peripheral positions, the left and right earlobe (LE, RE), left and right finger (LF, RF) and left and right toe (LT, RT), were selected to assess sLFOs characteristics, as shown in Fig. 2. Based on these characteristics of the peripheral positions, the concurrent CW fNIRS principle (CON-CW fNIRS) was proposed, whereby all the light sources with the same wavelength emit simultaneously, as shown in Fig. 2. Because of the wide distance between multiple peripheral channels (e.g., left and right finger), crosstalk is not a problem when simultaneous measurements are taken. CON-CW fNIRS systems use constant light intensity, which prevents additional demodulation circuitry. In addition, synchronous emission between channels can mitigate the time delay in studying sLFOs propagation characteristics. By comparing Figs. 1a and 2, in the CON-CW fNIRS system, the system's overall sampling frequency is independent of the number of channels. This ensures a high sampling frequency when multiple channels operate simultaneously. Finally, the finger-sleeve probe, which we adopted here, protects the measurement from ambient light interference and insures stable contact. During the experiment, the optical opacity of the experimental environment can be maintained by turning off the light or pulling the curtain, thus achieving optimal effects.

In the CON-CW fNIRS system, Δ[HbO] and Δ[Hb] levels are calculated by measuring the light intensity attenuated by body tissue. The modified Beer–Lambert law (MBLL) was used to translate the light intensity signals into Δ[HbO] and Δ[Hb] concentrations. The MBLL extends the Beer–Lambert law by introducing a scattering-dependent light intensity loss parameter, G. The calculation describes the oxygen saturation interacting with light intensity loss as a function of chromophore concentrations (c, units [M]), a molar extinction coefficient (ε, [M^{-1} cm^{-1}]), a differential path factor (DPF), source-detector distance (d, [cm]) and G. DPF and extinction coefficient can vary on tissue composition; therefore, users can select appropriate values according to different studies (e.g., forehead DPF (690 nm) ranges 5.6 to 6.9) [34].

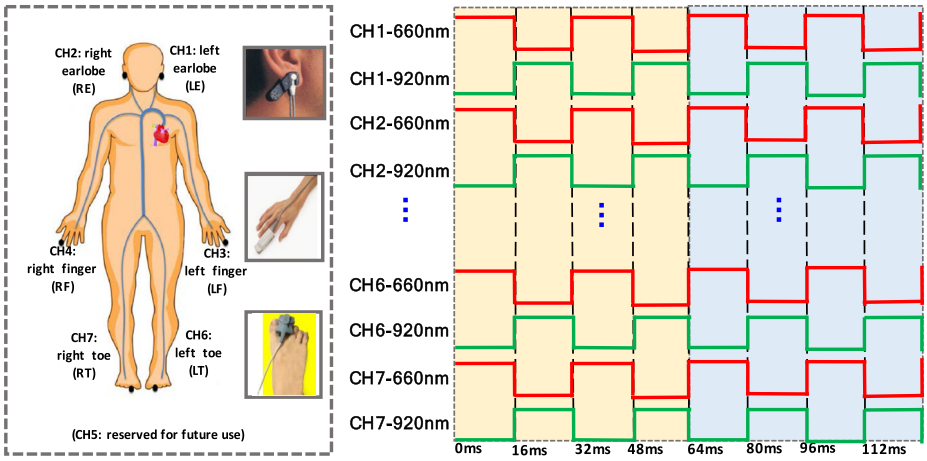

Fig. 2 Schematic setup and diagram of the CON-CW fNIRS system

$$\mathrm{OD}(t,\lambda) = -\log_{10}\left(\frac{I(t,\lambda)}{I_0(t,\lambda)}\right) = \sum\nolimits_i \varepsilon_i(\lambda)c_i(t)\mathrm{DPF}(\lambda)d + G(\lambda) \quad (1)$$

where the light intensity in the experiment is expressed as logarithm base 10. Thus, the molar extinction coefficient is used, instead of the absorption coefficient associated with the natural logarithm. Both the molar extinction coefficient and the absorption coefficient represent the absorption level per unit concentration. The molar absorption coefficient is equal to the molar extinction coefficient times 2.303 G. This can be ignored.

$$\mathrm{OD}(t,\lambda) = -\log_{10}\left(\frac{I(t,\lambda)}{I_0(t,\lambda)}\right) = \sum\nolimits_i \varepsilon_i(\lambda)c_i(t)\mathrm{DPF}(\lambda)d \quad (2)$$

The light intensity of the two wavelengths ($\lambda 1$, $\lambda 2$) is taken as the input variable to obtain the relative changes in the concentrations of oxygenated hemoglobin Δ[HbO] and deoxygenated hemoglobin Δ[Hb], respectively, as shown in Formula (3).

$$\begin{bmatrix} \Delta[\mathrm{Hb}] \\ \Delta[\mathrm{HbO}] \end{bmatrix} = (d)^{-1} \begin{bmatrix} \varepsilon_{\mathrm{Hb},\lambda_1} & \varepsilon_{\mathrm{HbO},\lambda_1} \\ \varepsilon_{\mathrm{Hb},\lambda_2} & \varepsilon_{\mathrm{HbO},\lambda_2} \end{bmatrix}^{-1} \begin{bmatrix} \Delta\mathrm{OD}(\Delta t,\lambda_1)/\mathrm{DPF}(\lambda_1) \\ \Delta\mathrm{OD}(\Delta t,\lambda_2)/\mathrm{DPF}(\lambda_2) \end{bmatrix} \quad (3)$$

3 Realizing low-power consumption with the MNO system

3.1 System design overview

Even though we have only six peripheral positions, where channels are required, the multichannel NIRS oximeter (MNO) established in this study comprises seven possible NIRS channels. The extra channel is included to test other candidate acquisition regions for specific studies. This is enough to measure transmission through the left and right ear lobes, left and right fingers and left and right toes (and a potential test site), at constant light intensities of 660 nm and 920 nm in a 32 ms cycle (IR:16 ms, VS:16 ms). Each MNO channel is an independent unit consisting of a two-stage input amplifier, with ADCs at the output of each stage and adjustable LED output power, as shown in Fig. 3.

We started from a reference design based on the Olimex board, but have since then completely rewritten the acquisition software and developed a new custom board for this purpose. MSP430FG439 was used as a microcontroller unit (MCU) featuring ultralow power. This contributed to the lower-power consumption in the MNO system. In the free run mode, the onboard MCU was reprogrammed to perform a rapid, closed-loop offset adjustment of the first amplifier stage to keep the 512 Hz digitized optical signals at a dithered target value. The offset waveforms were filtered and downsampled by a factor of 16, achieving 14 effective bits of dynamic range at 31.25 Hz with a flat frequency response (DC to 15.625 Hz) with a 12-bit ADC, namely MSP430 per 31.25 ms transfer data to Teensy. The Teensy 3.2 also generates a sample clock to synchronize the seven MSP430 boards.

The PIN diode signals are amplified by built-in operational amplifiers OA0 and OA1, and the ADC12 samples both amplifiers' outputs. The samples were correctly sequenced by the ADC12 hardware, and the MCU software separates the infrared and red components. Real-time samples are sent to the PC via Teensy and displayed on the PC for oxygen content. Apart from the MCU and the four transistors, only passive components are needed for this system design.

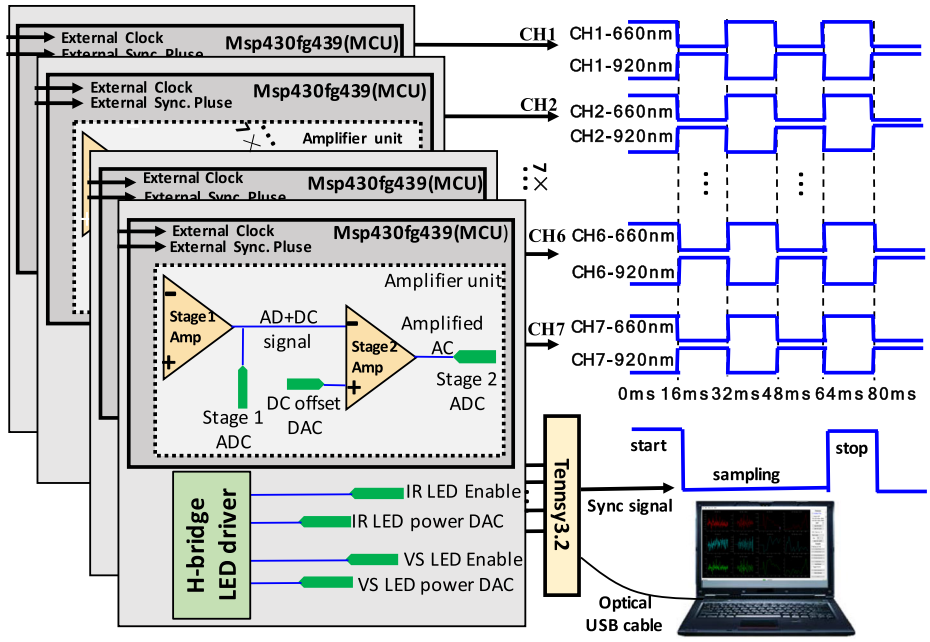

Fig. 3 The system consists of seven separate NIRS units, Teensy and a PC as well as the signal transmission mode in each channel

3.2 Single-channel NIRS oxmiter design specifications

3.2.1 Controlling the light source drive

Light source switch control and brightness adjustment control are the indispensable factors for determining the accuracy of the collected data in MNO operation. We note that this is a onetime adjustment prior to the beginning of the acquisition to maximize the dynamic range of the measurement in each channel. As described above, we do not modulate the LED intensity (other than to turn it on and off) during the course of the data acquisition. An H-bridge circuit was used in the MNO system to drive the light source. It was composed of four transistors (*T*1, *T*2, *T*3 and *T*4), as shown in Fig. 4b. In the Nellcor compatible probe, two LEDs were connected back to back. An H-bridge circuit was connected to the probe interfaces to drive the 660 nm and 920 nm LEDs. A DAC0 controlled the current, and its light output level, through LEDs. The 12-bit DAC0 can be connected to either pin 5 or pin 10 of the MCU through computerized control in the DAC control register. When a pin is not chosen to output the DAC0 signal, it is set to Hi-Z or low. The base of each transistor has a pull-down resistor to ensure the transistor is off when it is not selected. Timer A controls the multiplex sequence and automatically starts the ADC conversion. At the CCR0 interrupt, a new LED sequence is initiated with the following. The DAC12_0 control bit DAC12OPS is set or cleared, depending on which LED is driven; a new value for DAC12_0 is set to the corresponding light intensity level; DAC12_1 is set to the DC tracking filter output for that particular LED.

The four-transistor H-Bridge is a variable gain circuit that turns the LEDs on and off. This arrangement consumes a significant portion of the total current, as shown in Fig. 4c, d. However, the amount of current consumed depends on the DAC0 output that is used to turn on transistors. The DAC0 output controls the light intensities of the LEDs such that they are well within the pre-determined target range. The light intensity control is computerized by comparing the LED light intensities previously sampled with the target high and low thresholds. Fine or coarse step counts guide the LED intensity back in the right direction when LED intensity exceeds the target range. Then the DAC0_DAT register is loaded with appropriate data. The LED light intensities need to be high, because weak signals degrade the results in later stages. Because the value of the DAC12_ODAT register changes depending on the previously sampled data points, the pulsoximeter board's current consumption can vary. For the ease of current consumption computation, the operation of the four-transistor H-Bridge can be classified into two cases. These cases represent the two extreme H-Bridge current consumption scenarios. As shown in Fig. 4c, when DAC_12OPS bit = 1, the IR LED is on, the current flows through transistors *T*3 and *T*2, and *T*3's base current is 0.23 mA. *T*2's transmitter current has two states—the lowest current is 3 mA, and the highest current is 36 mA. As shown in Fig. 4d, when DAC_12OPS bit = 0, the VS LED is on, the current flows through transistors *T*1 and *T*4, *T*1's base current is 0.23 mA, *T*4's base current has two states, the lowest current is 0.15 mA and the highest current is 0.27 mA. In run mode, when the

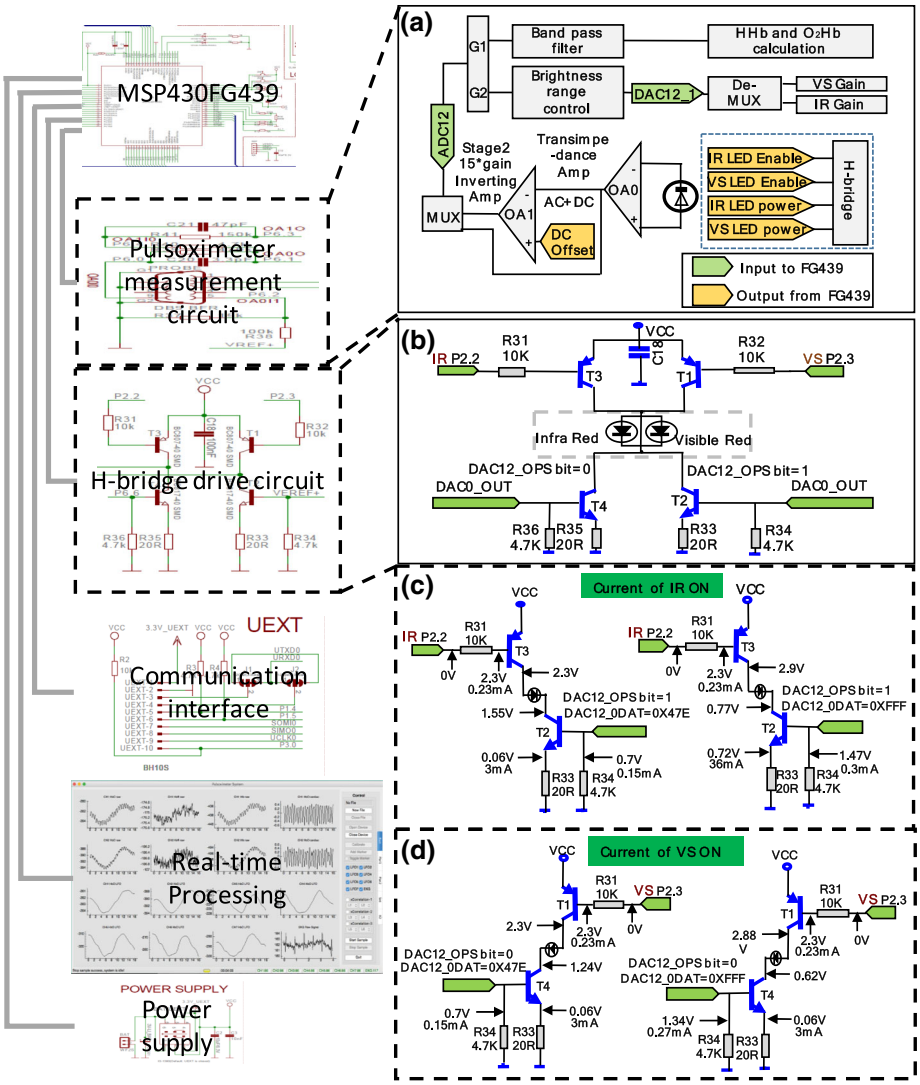

Fig. 4 Schematic diagram of the MCU design in the MNO, illustrating the MCU circuit's layout (**a**), the H-bridge circuit (**b**) and the H-bridge circuit's current consumption in the state of IR on (**c**) and VS on (**d**)

LED value = 2047, the power consumption of each MOD-pulse board is 14 mA, and the power consumption of 7 MOD-pulse boards is 14 mA × 7 = 98 mA; when the LED value ≥ 3172, the power consumption of each MOD-pulse board is 25 mA and the power consumption of 7 MOD-pulse boards is 25 mA × 7 = 175 mA.

Low-power mode (LPM) operation is a vital feature of MSP430. This provides a tiny current drain when the processor is in standby mode. Several low-power modes are supported, which balance the needs of different applications. As the number of LPM modes increases, the number of components that are disabled on the chip increases. The active mode is not a low-power mode, but rather a mode in which all components are turned on, with the possible exception of some peripherals. In LPM0 mode, the CPU and MCLK are off and the SMCLK and ACLK remain active. In LPM1 mode, the CPU and MCLK are off, but the DCO and DC generators are disabled if the DCO is not used for SMCLK. In LPM2 mode, the CPU, MCLK, SMCLK and DCO are disabled, while the DC generator is still enabled. In the LPM3 mode, the CPU, MCLK, SMCLK, DCO and DC generators are disabled. In the LPM4 mode, the CPU and all of the clocks are disabled. When it is in low-power LPM0 mode, MSP430 will halt, but MSP430 will respond to the interruption.

3.2.2 NIRS signal acquisition and processing

The light signals transmitted through tissue were collected in the photodiode, which was converted to the amplified voltage signal by a transimpedance amplifier (OA0) whose output signal consisted of DC and AC. Among them, AC includes sLFOs signal components, while DC contains mostly motion artifact and ambient light noise, which are not sLFOs. If the subjects move their fingers during the experiment, the waveform of the OA0 output signal changes under the influence of the motion artifact. The OA0 output signal is sensitive to motion artifact and

ambient light noise, so although the OA0 output signal includes the original sLFOs, this part of the signal needs to be adjusted and cannot be used directly. The high and low thresholds for the OA0 output for the fine turn are 3800 and 2700, respectively. By adjusting the LED strength at the beginning of the experiment, the OA0 output signal value is kept within the target range; its exact value is not important and only needs to be high, because a weak signal will generate terrible results in the later stage (OA1). However, the exact value only has to be within the range that can be handled by the next stage (OA1). The circuit design of the two-stage input amplifier is shown in Fig. 4a.

The second-stage amplifier (OA1) is a differential amplifier used to adjust the OA0 output signal. OA1 has two modes: internal resistors and external resistors. When OA1 uses external parameters (R40 = 4.7 K, R41 = 150 K), the purpose of which is operational amplification, the gain is about 32. By default, OA1 uses internal resistors (R40 = R, R41 = 15R). The OA1 mode and gain are all valid (not zero) in this mode. As an inverse feedback amplifier, the internal OA1gain is 15, as shown in Fig. 4a. The amplifying OA1 circuit can be calculated as:

$$\frac{V_{\mathrm{IR\_Stage1}} - V_{\mathrm{IR\_DC\_Offset}}}{R1} = \frac{V_{\mathrm{IR\_DC\_Offset}} - V_{\mathrm{IR\_Stage1}}}{R2} \tag{4}$$

$$\frac{V_{\mathrm{VS\_Stage1}} - V_{\mathrm{VS\_DC\_Offset}}}{R1} = \frac{V_{\mathrm{VS\_DC\_Offset}} - V_{\mathrm{VS\_Stage1}}}{R2} \tag{5}$$

According to the OA1 internal resistance parameters, the output voltage values for IR and VS can be constructed as:

$$V_{\mathrm{IR\_Stage2}} = 16V_{\mathrm{IR\_DC\_Offset}} - 15V_{\mathrm{IR\_Stage1}} \tag{6}$$

$$V_{\mathrm{VS\_Stage2}} = 16V_{\mathrm{VS\_DC\_Offset}} - 15V_{\mathrm{VS\_Stage1}} \tag{7}$$

$V_{\mathrm{IR\_Stage2}}$ and $V_{\mathrm{VS\_Stage2}}$ are the OA1 voltage IR and VS values, respectively; $V_{\mathrm{IR\_DC\_Offset}}$ and $V_{\mathrm{VS\_DC\_Offset}}$ are the IR DC offset and the VS DC offset output by DC tracker; $V_{\mathrm{IR\_Stage1}}$ and $V_{\mathrm{VS\_Stage1}}$ are the IR voltage values and the VS voltage values output by OA0, respectively.

The OA1 output voltage is around 2047; the ADC resolution is 12 bits; the max sample value is 4095 and the middle value is 2047. The reference for ADC is 2.5 V, and the target output voltage of OA1 is 1.25 V. In this study, the sampling frequency was downsampled from 1000 to 32 Hz for IR LED and VS LED with 16 sample cycles. Therefore, the OA1 target value was 16 times per sample circle and needed dynamic adjustment of the OA1 output value to get the target value. Based on the above analysis, the original IR and VS signals can be calculated as:

$$\begin{aligned}\mathrm{IR\_Raw\_Signal} = {} & (15\mathrm{IR\_DC\_Offset} \\ & -(\mathrm{IR\_Error\_Signal} - S2\_\mathrm{Target}))/2^4\end{aligned} \tag{8}$$

$$\begin{aligned}\mathrm{VS\_Raw\_Signal} = {} & (15\mathrm{VS\_DC\_Offset} \\ & -(\mathrm{VS\_Error\_Signal} - S2\_\mathrm{Target}))/2^4\end{aligned} \tag{9}$$

Among them, IR_Error_Signal is $V_{\mathrm{IR\_Stage2}}$, VS_Error_Signal is $V_{\mathrm{vs\_Stage2}}$, IR_DC_Offset is $V_{\mathrm{IR\_DC\_Offset}}$ and VS_DC_Offset is $V_{\mathrm{VS\_DC\_Offset}}$. Formulae (6), (7), (8)and (9) were calculated simultaneously as:

$$\begin{aligned}\mathrm{IR\_Raw\_Signal} = {} & (15\mathrm{IR\_Stage1} \\ & -\mathrm{IR\_DC\_Offset} + S2\_\mathrm{Target})/2^4\end{aligned} \tag{10}$$

$$\begin{aligned}\mathrm{VS\_Raw\_Signal} = {} & (15\mathrm{VS\_Stage1} \\ & -\mathrm{VS\_DC\_Offset} + S2\_\mathrm{Target})/2^4\end{aligned} \tag{11}$$

The raw signal comes from IR_Stage1 and is adjusted with IR_DC_Offset and S2_Target. Because S2_Target fluctuates, it is appropriate to determine the target value is 2047 in the final formula. Thus, the original signal can be calculated as:

$$\begin{aligned}\mathrm{IR\_Raw\_Signal} = {} & \left(2^4\mathrm{IR\_DC\_Offset}\right. \\ & \left.-\mathrm{IR\_Error\_Signal}\right)/2^4\end{aligned} \tag{12}$$

$$\begin{aligned}\mathrm{VS\_Raw\_Signal} = {} & \left(2^4\mathrm{VS\_DC\_Offset}\right. \\ & \left.-\mathrm{VS\_Error\_Signal}\right)/2^4\end{aligned} \tag{13}$$

The original light intensity signal is obtained by amplifying the DC offset by a factor of 16 (4 bits to the left) and subtracting the OA1 voltage value, then dividing the obtained values by 16 (4 bits to the right). The two-stage amplifying circuit can remove the noise signal and extract the original physiological signal.

3.3 Multi-channel cascade and transport protocol design

The design of the special transmission protocol for solving the multi-channel data transmission problem is crucial to upgrade the single-channel NIRS oximeter to multi-channel. There are 7 NIRS channels in the MNO system, and the communication connection between the Teensy and the seven MSP430 boards is shown in Fig. 5b. By using a serial bus, the Teensy sends commands to seven boards. However, only one board responds and sends sample data to the Teensy. To avoid confusion in serial bus data transmission, seven 1N4148 diodes are used for isolation. 32 bytes can be transmitted in MSP430 boards (16 IRs and 16VSs), and thus queuedata have to be executed. Because the power line filter takes up a lot of time, the queuedata function lasts about 10 ms.

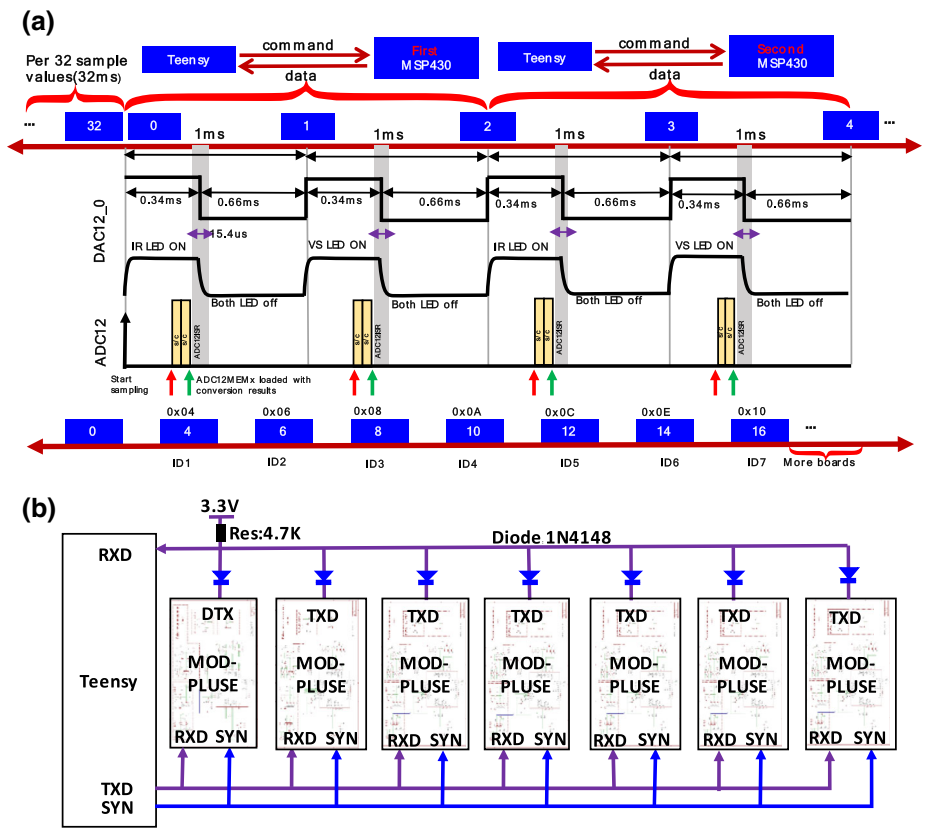

Fig. 5 **a** Communication protocol and **b** communication connection between the Teensy and the seven MOD-pulse boards

The address of the seven MSP430 boards is 1–7, and the commands to the MSP430 boards consist of a single byte address (1–7) and a single byte opcode from the list 1, 2, 3, 4, 9, A, B, C and D. Commands 1, 2, 3 and 4 are common commands, such as self-test, start sample and stop sample. When 7 MSP430 boards receive the commands through serial bus, they cannot process them if the address is not 1–7. The Teensy then sends commands to each MSP430 board. When the MSP430 board receives the command from the Teensy, MSP430 immediately sends data to the Teensy for feedback. The duration of this operational process is about 4 ms. After this communication, the Teensy continues to send commands to the next board and the overall process with time-sharing characteristics. The Teensy to MSP430 communication protocol is shown in Fig. 5a.

In the free run mode, MSP430 receives no request data command from the Teensy. When receiving the start sample command, MSP430 has to automatically send data to the Teensy. When MSP430 has sampled 32 values, MCU need to execute queue data command queuedata function after entering ISR. MCU enters ISR twice in the process, and the queuedata function running time is between 2 and 3 ms. When executing the xmitdata function that sends data through the serial port, the MCU also enters the ISR twice. This can be proven by the serial transmission bandwidth. 22 bytes of data needs to be transferred into xmitdata with a bandwidth of 115,200, and the total time is $22 \times (8 + 1 + 1)/115{,}200 = 1.9$ ms, combined with a start and stop bit. This study assumes that the TimeA interrupt is entered a maximum of 3 and a minimum of 2.5 times, and the number of boards MNO can connect is $9.6 = (32–3)/3 <$ number of boards $< 11.8 = (32–2.5)/2.5$.

Synchronous signal indicates that the Teensy knows the time MSP430 started sampling and the time MSP430 transferred data for feedback. To prevent data loss, the Teensy must send a request data command to MSP430 immediately after starting the sample or transferring the data to the host. Thus, when the MSP430 data are available, it is sent to the Teensy immediately. There are two mechanisms for transferring data to the Teensy. The MSP430 has 31.25 ms to transfer a data frame to avoid data loss. Thus, if the Teensy does not receive the data within 32 ms, a time out error occurs, and stop sample should be run. The MSP430 package contains 18 bytes. To prevent MSP430 from transferring too much data (over 18 bytes), when the Teensy has received 18 bytes, it will delay 4 ms. If the data consist of 18 bytes and the Teensy has no errors, then the MSP430 package data are correct. The transmitted data can then be displayed in real time in the

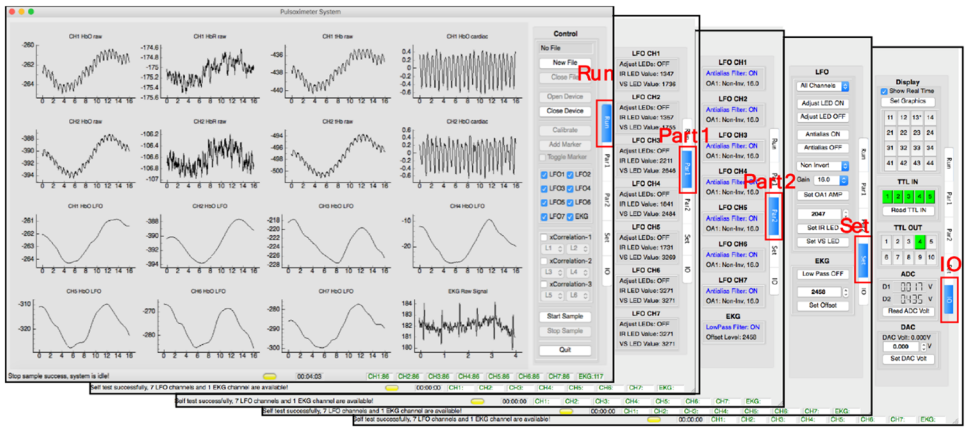

Fig. 6 The user-interface in five states shows real-time changes in Δ[HbO], Δ[Hb] and sLFOs data

upper computer interface, as shown in Fig. 6. The light intensity signal collected by the MNO device is converted into Δ[HbO] and Δ[Hb] and anaerobic hemoglobin through real-time processing in a multithreaded Python program on the host computer. Therefore, the MNO device can display sLFOs in real time after filtering (0.01–0.15 Hz), and users can also save the raw light intensity signal according to their needs for offline processing. The user-interface in five states shows real-time changes in Δ[HbO], Δ[Hb] and sLFOs data. In the run state, the display shows real-time changes in Δ[Hb], Δ[Hb] and sLFOs data. Part1 and Part2 show the parameter setting status of the device. Set and IO are used for device parameter setting and window display setting, respectively.

3.4 Equipment components and appearance implementation

In order to facilitate the application of MNO in more occasions, the MCU design is improved on the basis of MOD-pulse hardware and integrated again with length: 56.87 mm, width: 40.91 mm, as shown in Fig. 7a, b. Openscad was used to design a 3D external box for MNO system. The box for the MNO equipment is divided into two main components consisting of sliding units and an equipment frame. MOD-pulse boards are affixed in each sliding unit for blood oxygen detection. A total of seven NIRS sliding units (CH1-CH7) were designed in the MNO box, as shown in Fig. 7c. A Teensy sliding unit can also be designed in the MNO box alone. The shell dimensions of the equipment are $10 \times 10 \times 20$ cm^3, which is smaller than the currently smallest fNIRS device (NIRSport). Its

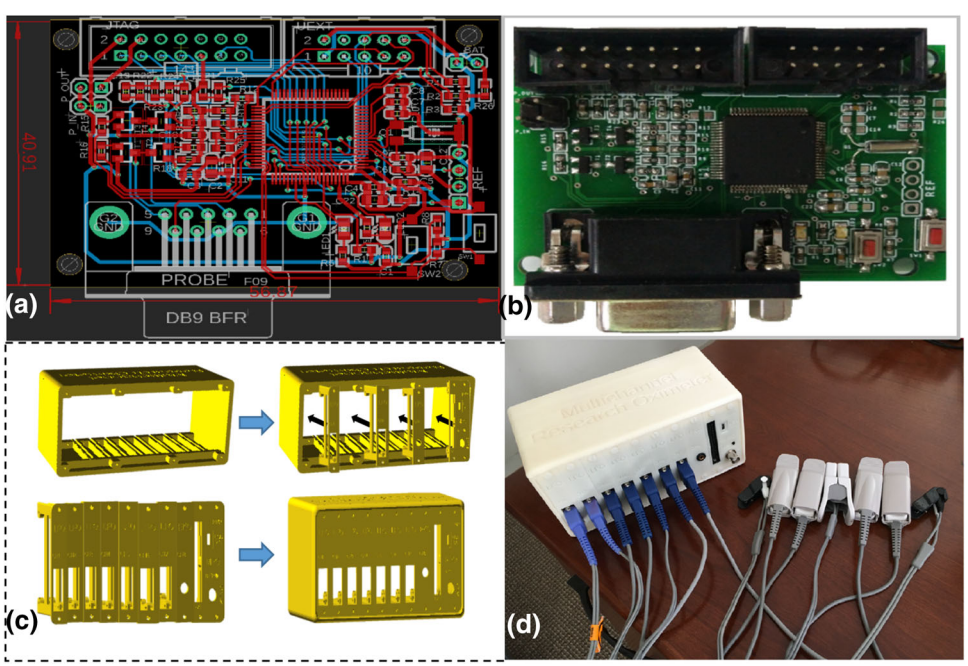

Fig. 7 PCB design in the MNO equipment (**a**), the completed MCU board (**b**), external design of the MNO equipment (**c**) and completed MNO equipment (**d**)

Table 1 Component costs for building system (consisting 7 MOD-pulse); the total is ~ $288 excluding the NIRS probe

Component	Description	Price
Python 2.6 (including numpy, scipy, matplotlib, and serial libraries)	Used on the host computer to handle USB communication with the MNO spectrometer, and to preprocess, display and store data	Free
MSP430-gcc toolchain	C compiler for use with MSP430 microcontrollers (used to program the MOD-pulse)	Free
Olimex USB JTAG programmer	This device is used to download new firmware to the MOD-pulse board (or any other JTAG compatible development board)	US $75
Equipment shell	The MNO device shell includes a multi-channel box and seven mod-pulse sled. We have designed a case that can be printed on a rapid prototyping machine for rugged and inexpensive construction. The price listed is an estimate of our material cost on a Dimension uPrint 3D printer	US $20
Olimex MOD-pulse pulse oximeter development board	A programmable Texas Instruments MSP430FG439 development board which implements TI's reference design for a Nellcor-compatible single chip pulse oximeter	US $21.9
Nellcor compatible pulse oximeter sensor	Two wavelength (660 nm and 920 nm) source-detector pair with medical connector. There are hundreds of compatible probes (both reusable and disposable) available for use in different body locations and populations	US $10–300
Tennsy3.2	An optical communications unit for acquisition control and data transmission	US $19.8
10 pin ribbon cable, USB cable, screws	Board interconnects, device to computer connection, hardware to secure boards to case	US $10

compactness and portability can be applied to various experiments and might be highly advantages if used in clinical settings or as bed-side technique. The diagram of the assembled MNO equipment is shown in Fig. 7d.

Funane et al. concluded from their theoretical analysis that optimal results can be acquired when both ends of the range of 659–900 nm were used [35]. Therefore, dedicated medical probes with 660 nm and 920 nm LED light were selected for the device probe source. As mentioned above, the probe is sturdy and can be affixed to the fingers, toes or earlobes position with steady contact, mitigating the influence of ambient light noise. In addition, the MNO equipment proposed in this study is highly cost-effective. One-time hardware and software costs required to program and operate the device total $75. Component costs to build seven units (consisting of 7 MOD-pulses) totaled ~ $213. The total cost of the equipment is ~ $288, as shown in Table 1. The low cost of MNO reduces the financial burden on researchers and make the MNO device suitable for widespread use.

4 The MNO system's accuracy verification

In order verify the accuracy of our measurements, we compared our MNO device with the ISS (ISS Imagent, Champaign, IL) a commercial fNIRS device, by direct comparison ($N = 1$) and comparison of time delay (T_{delay}) and maximum cross-correlation (r_{max}) values with previously published data on a commercial fNIRS device. The ISS is a near-infrared tissue imager comprising 16 laser sources at 690 and 830 nm and four optical detectors. Each probe includes one collection fiber and one pair of illumination fibers (690 and 830 nm). The separation between the collection and illumination fibers was 1.5 cm. The sampling rate of the ISS data acquisition was 12.5 Hz in order to fully sample the cardiac waveform.

For our direct comparison, the probes of the ISS and the MNO were placed over the tip of participant's right hand middle and index finger, respectively, as shown in Fig. 8a. In the direct comparison experiment of the ISS and our MNO device, ISS data (right hand middle finger) and MNO data (right hand index finger) of the same participant were recorded simultaneously, as shown in Fig. 8a. Signals were collected simultaneously and converted into Δ[HbO] and Δ[Hb] signals by the Beer-Lambert law. The MNO data were first downsampled from 31.25 to 12.5 Hz to match the ISS data. ISS data and MNO data were then normalized to acquire optimal comparison, as shown in Fig. 8b, c. The correlation coefficients between the ISS and our MNO are 0.908 and 0.841 for Δ[HbO] and Δ[Hb], respectively. Figure 8d, e shows the power spectra from the two devices, displaying the similar frequency responses of the devices. By band-pass filtering (0.01–0.15 Hz) Δ[HbO] and Δ[Hb] to sLFOs, we extracted LFO(Δ[HbO]) and LFO(Δ[Hb]), as shown in Fig. 8f, g. The correlation coefficients of LFO(Δ[HbO]) and LFO(Δ[Hb]), acquired using the ISS and MNO, are 0.905 and 0.671, respectively. Δ[HbO] was highly comparable between the instruments. Δ[Hb] was less well correlated, which is expected considering that in vivo, Δ[HbO] has approximately 30 times the concentration of Δ[HHb] and therefore much higher signal-to-noise.

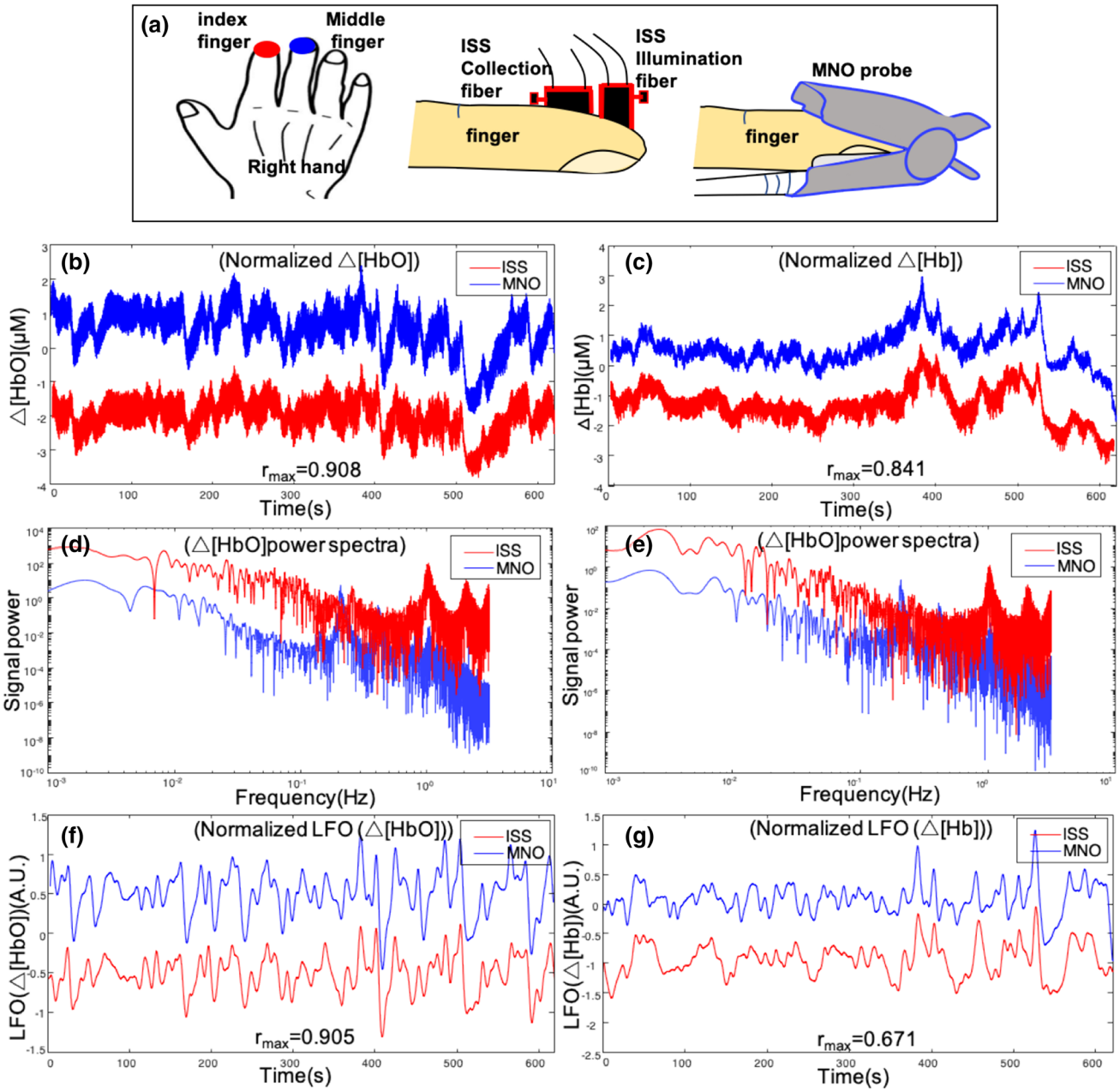

Fig. 8 Methods and positions (**a**) of detecting Δ[HbO] and Δ[Hb] using the ISS and our MNO device. Δ[HbO] (**b**) and Δ[Hb] (**c**) time course observed with the ISS and our MNO device and the corresponding power spectra of Δ[HbO] (**d**) and Δ[Hb] (**e**). Corresponding LFO(Δ[HbO]) (**d**) and LFO(Δ[Hb]) (**e**) were obtained after band-pass filtering (0.01–0.15 Hz)

For further verification, we collected data from 25 healthy individuals (21–57 years old; 12F, 13 M) with our MNO device in the periphery (fingers and toes) and compared our results with previously published data on the ISS [1]. The correlation coefficients and time delays of the LFO (ΔHbO) signal between left and right toes (LT-RT) as well as left finger and left toe (LF-LT) were calculated [36]. The maximum correlation coefficient between toes (LT-RT) was $r = 0.89 \pm 0.06$, with time delays of 0.61 ± 0.87 s; the maximum correlation coefficient between left finger and left toe (LF-LT) was $r = 0.61 \pm 0.13$, with time delays of -6.62 ± 4.7 s, as shown in Table 2. The time delays and maximum correlation coefficients are within the range of values published previously with the ISS equipment in healthy subjects, including under 2 s delay and > 0.8 maximum correlation coefficient between symmetrical sites (e.g., LT-RT) and slightly lower correlation ($r = \sim 0.7$) and greater delays between finger and toes [1]. The results above show that the data collected by our MNO

Table 2 A summary of maximum cross-correlations (r_{max}) and time delays (T_{delay}) of ISS results (N = 6/3) and MNO results (N = 25). The group mean ± SD is shown

Name	Previously published ISS results [1]	CON-CW fNIRS/ MNO results [36]
Hemoglobin	△[tHb]	△[HbO]
LF-LT		
Number (N)	N = 6	N = 25
	(30 ± 7 years, 3F)	(21–57 years, 12F)
(Maximum cross-correlations) (r_{max})	0.70 ± 0.08	0.61 ± 0.13
(Time delays) (T_{delay})	3.07 ± 0.81 s	− 6.62 ± 4.68
LT-RT		
Number (N)	N = 3	N = 25
(Maximum cross-correlations) (r_{max})	0.85 ± 0.09	0.89 ± 0.06
(Time delays) (T_{delay})	− 0.02 ± 0.57 s	0.61 ± 0.87 s

equipment have high reproducibility and are comparable to commercial fNIRS devices.

5 Conclusion

This paper proposes a portable, energy-efficient, low-cost and multichannel NIRS oximeter [MNO] for synchronizing sLFOs detection at multiple positions in the periphery. The concurrent continuous wave fNIRS system (CON-CW fNIRS) is proposed and used in the MNO system according to the characteristics of human peripheral positions. The MNO has seven NIRS channels through which the sLFOs characteristic in peripheral positions (fingers, toes, earlobes) can be more comprehensively revealed. In addition, special medical probes were used for the MNO for optimal applicability in experimental and clinical research. The low cost of the MNO reduces the financial burden for researchers, and its portability makes it suitable for more experimental environments. We showed that our MNO device is highly correlated with commercial devices such as the ISS, by direct comparison and comparison of delay and correlation values with previously published data. These combined advantages contribute to the MNO device characteristics that make them suitable for widespread use.

Acknowledgements This work was supported by the National Natural Science Foundation of China (61827811), the Hebei Provincial Education Department's support plan (SLRC2019042) and by the National Institutes of Health, Grants K25 DA031769, R01 NS097512.

Compliance with ethical standards

Conflict of interest The authors have no relevant financial interests in this article and no potential conflicts of interest to disclose.

References

1. Tong Y et al (2012) Low-frequency oscillations measured in the periphery with near-infrared spectroscopy are strongly correlated with blood oxygen level-dependent functional magnetic resonance imaging signals. J Biomed Opt 17(10):106004
2. Livera LN et al (1992) Cyclical fluctuations in cerebral blood volume. Arch Dis Child 67(1 Spec No):62–63
3. Hoshi Y et al (1998) Relationship between fluctuations in the cerebral hemoglobin oxygenation state and neuronal activity under resting conditions in man. Neurosci Lett 245(3):147–150
4. Elwell CE et al (1999) Oscillations in cerebral haemodynamics: implications for functional activation studies. Adv Exp Med Biol 471:57–65
5. Katura T et al (2006) Quantitative evaluation of interrelations between spontaneous low-frequency oscillations in cerebral hemodynamics and systemic cardiovascular dynamics. NeuroImage 31(4):1592–1600
6. Tass P et al (1998) Detection of n: m phase locking from noisy data: application to magneto-encephalography. Phys Rev Lett 81(15):3291–3294
7. Gagnon L et al (2012) Quantification of the cortical contribution to the NIRS signal over the motor cortex using concurrent NIRS-fMRI measurements. NeuroImage 59(4):3933–3940
8. Kirilina E et al (2012) The physiological origin of task-evoked systemic artefacts in functional near infrared spectroscopy. NeuroImage 61(1):70–81
9. Tong Y et al (2011) Isolating the sources of widespread physiological fluctuations in functional near-infrared spectroscopy signals. J Biomed Opt 16(10):106005
10. Donahue MJ et al (2016) Time delay processing of hypercapnic fMRI allows quantitative parameterization of cerebrovascular reactivity and blood flow delays. J Cereb Blood Flow Metab 36(10):1767–1779
11. Sassaroli A et al (2012) Low-frequency spontaneous oscillations of cerebral hemodynamics investigated with near-infrared spectroscopy: a review. IEEE J Sel Top Quantum Electron 18(4):1478–1492
12. Medvedev AV (2014) Does the resting state connectivity have hemispheric asymmetry? A near-infrared spectroscopy study. NeuroImage 85(1):400–407
13. Niu H et al (2013) Test-retest reliability of graph metrics in functional brain networks: a resting-state fNIRS study. PLoS ONE 8(9):e72425
14. Karim HT et al (2013) Neuroimaging to detect cortical projection of vestibular response to caloric stimulation in young and older adults using functional near-infrared spectroscopy (fNIRS). NeuroImage 76:1–10
15. Franceschini MA et al (2003) Hemodynamic evoked response of the sensorimotor cortex measured noninvasively with near-infrared optical imaging. Psychophysiology 40(4):548–560
16. Peltonen JE et al (2012) Alveolar gas exchange and tissue deoxygenation during exercise in type 1 diabetes patients and healthy controls. Respir Physiol Neurobiol 181(3):267–276
17. Anwar RA et al (2013) Comparison of causality analysis on simultaneously measured fMRI d NIRS signals during motor tasks. In: Conference proceedings: annual international conference of the IEEE Engineering in medicine and biology society.

IEEE engineering in medicine and biology society. conference, pp 2628–2631
18. Haigh SM et al (2015) Cortical excitability and the shape of the haemodynamic response. NeuroImage 111:379–384
19. Li H et al (2012) Lipschitz-Killing curvature based expected Euler characteristics for p-value correction in fNIRS. J Neurosci Methods 204(1):61–67
20. Nieuwhof F et al (2016) Measuring prefrontal cortical activity during dual task walking in patients with Parkinson's disease: feasibility of using a new portable fNIRS device. Pilot Feasibility Stud 2(1):918719
21. Jin SH et al (2018) NIRS-based experimental evaluation of driver back fatigue during long-term driving. Biotechnol Biotechnol Equip 32(3):804–814
22. Jeppesen J et al (2015) Exploring the capability of wireless near infrared spectroscopy as a portable seizure detection device for epilepsy patients. Seizure 26:43–48
23. Maidan I et al (2016) The role of the frontal lobe in complex walking among patients with Parkinson's disease and healthy older adults: an fNIRS study. Neurorehabil Neural Repair 30(10):963–971
24. Maidan I et al (2017) When is higher level cognitive control needed for locomotor tasks among patients with parkinson's disease? Brain Topogr 30(4):531–538
25. Xu J et al (2015) FC-NIRS: a functional connectivity analysis tool for near-infrared spectroscopy data. Biomed Res Int 2015:1–11
26. Nakanishi Y et al (2017) Differential therapeutic effects of atomoxetine and methylphenidate in childhood attention deficit/hyperactivity disorder as measured by near-infrared spectroscopy. Child Adolescent Psychiatry Mental Health 11(1):26
27. Homae F et al (2010) Development of global cortical networks in early infancy. J Neurosci 30(14):4877–4882
28. Taga G et al (2011) Spatiotemporal properties of cortical haemodynamic response to auditory stimuli in sleeping infants revealed by multi-channel near-infrared spectroscopy. Philos Trans R Soc A 369(1955):4495–4511
29. Grossmann T et al (2018) The neurodevelopmental precursors of altruistic behavior in infancy. PLoS Biol 16(9):e2005281
30. Chuang CH et al (2018) Brain electrodynamic and hemodynamic signatures against fatigue during driving. Front Neurosci 12:181
31. Shin J et al (2018) Simultaneous acquisition of EEG and NIRS during cognitive tasks for an open access dataset. Sci Data 5:180003
32. Berger A et al (2018) Brain oscillatory and hemodynamic activity in a bimanual coordination task following transcranial alternating current stimulation (tACS): a combined EEG-fNIRS study. Front Behav Neurosci 12:67
33. Perry S et al (2017) Getting to the root of fine motor skill performance in dentistry: brain activity during dental tasks in a virtual reality haptic simulation. J Med Internet Res 19(12):e371
34. Scholkmann F et al (2013) General equation for the differential pathlength factor of the frontal human head depending on wavelength and age. J Biomed Opt 18(10):105004
35. Schojkmann F et al (2014) A review on continuous wave functional near-infraed spectroscopy and imaging instrumentation and methodology. NeuroImage 85(1):6–27
36. Li Y et al (2018) Systemic low-frequency oscillations observed in the periphery of healthy human subjects. J Biomed Opt 23(5):1–11